



Impact of clouds on atmospheric heating based on the R04 CloudSat fluxes and heating rates data set

Tristan S. L'Ecuyer,¹ Norman B. Wood,¹ Taryn Haladay,¹ Graeme L. Stephens,¹ and Paul W. Stackhouse Jr.²

Received 11 February 2008; revised 5 June 2008; accepted 26 August 2008; published 6 December 2008.

[1] Among the largest uncertainties in quantifying the radiative impacts of clouds are those that arise from the inherent difficulty in precisely specifying the vertical distribution of cloud optical properties using passive satellite measurements. Motivated by the need to address this problem, CloudSat was launched in April 2006 carrying into orbit the first millimeter wavelength cloud radar to be flown in space. Retrieved profiles of liquid and ice cloud microphysical properties from this Cloud Profiling Radar form the basis of the CloudSat's fluxes and heating rates algorithm, 2B-FLXHR, a standard product that provides high vertical resolution profiles of radiative fluxes and atmospheric heating rates on the global scale. This paper describes the physical basis of the 2B-FLXHR algorithm and documents the first year of 2B-FLXHR data in the context of assessing the radiative impact of clouds on global and regional scales. The analysis confirms that cloud contributions to atmospheric radiative heating are small on the global scale because of a cancelation of the much larger regional heating from high clouds in the tropics and cooling from low clouds at higher latitudes. Preliminary efforts to assess the accuracy of the 2B-FLXHR product using coincident CERES data demonstrate that outgoing longwave fluxes are better represented than those in the shortwave but both exhibit good agreement with CERES on scales longer than 5 days and larger than 5°. Colocated CALIPSO observations of clouds that are undetected by CloudSat further indicate that while thin cirrus can introduce modest uncertainty in the products, low clouds that are obscured by ground clutter represent a far more important source of error in the current 2B-FLXHR product that must be addressed in subsequent versions of the algorithm.

Citation: L'Ecuyer, T. S., N. B. Wood, T. Haladay, G. L. Stephens, and P. W. Stackhouse Jr. (2008), Impact of clouds on atmospheric heating based on the R04 CloudSat fluxes and heating rates data set, *J. Geophys. Res.*, 113, D00A15, doi:10.1029/2008JD009951.

1. Introduction

[2] Clouds can significantly impact the development and maintenance of global circulations through their interaction with solar and terrestrial radiation [Hartmann and Short, 1980; Liebmann and Hartmann, 1982]. Regional differences in the character of clouds and precipitation play a significant role in defining the Earth's climate influencing everything from tropical upper tropospheric circulation patterns [Slingo and Slingo, 1988, 1991], to the propagation speed of tropical intraseasonal oscillations [Lee *et al.*, 2001], and the evolution of extratropical cyclones [Weaver, 1999]. Dating back to the early work of Vonder Haar and Suomi [1971], quantifying the impact of clouds on the Earth's radiation budget (ERB) has been the subject of vigorous research and has been among the primary objectives of numerous satellite platforms from Nimbus 7

through the Earth's Radiation Budget Satellite (ERBS) [Barkstrom, 1984] and Scanner for Radiation Budget (ScaRaB) missions [Kandel *et al.*, 1998] to the present day Geostationary Earth Radiation Budget (GERB) aboard the Meteosat Second Generation (MSG) satellite [Harries *et al.*, 2005] and Clouds and the Earth's Radiant Energy System (CERES) aboard Aqua and Terra [Wielicki *et al.*, 1996].

[3] Many studies have sought to make use of data acquired from these platforms to relate variability in the ERB to corresponding changes in cloud character and amount [e.g., Sohn and Smith, 1992a, 1992b, 1992c; Stephens and Greenwald, 1991a, 1991b; Hartmann *et al.*, 1992; Gupta *et al.*, 1993; Ringer and Shine, 1997; Moore and Vonder Haar, 2001]. Satellite observations of top of the atmosphere fluxes have also been used to derive shortwave radiation budgets at the surface [e.g., Li *et al.*, 1993; Breon *et al.*, 1994; Ba *et al.*, 2001a, 2001b; Hatzianastassiou and Vardavas, 2001]. Most recently the CERES [Wielicki *et al.*, 1996, 2001] Surface and Atmospheric Radiation Budget (SARB) working group have developed an approach to estimate TOA and surface fluxes by constraining atmospheric properties used in broadband flux calculations to

¹Department of Atmospheric Science, Colorado State University, Fort Collins, Colorado, USA.

²NASA Langley Research Center, Hampton, Virginia, USA.

agree with observed TOA fluxes (the most up-to-date information regarding SARB can be found at <http://www-surf.larc.nasa.gov/surf/>). Rossow and Lacis [1990], Zhang et al. [1995], Rossow and Zhang [1995], Bishop et al. [1997], and Chen et al. [2000] detail the evolution of an alternate technique that focuses first on the characterization of high and low cloud distributions from the International Satellite Cloud Climatology Project (ISCCP) and models their impact on the ERB using broadband flux calculations. While following somewhat different paths, these projects represent two of the most state-of-the-art methods for diagnosing a complete ERB, to date.

[4] As noted by Stephens et al. [2002], CloudSat adds a “new dimension” to cloud and precipitation retrievals from space-based platforms providing for the first time a means to assess vertical distributions of the properties of most types of clouds around the planet using reflectivity measurements from the 94 GHz Cloud Profiling Radar (CPR). This new information offers the potential to make new advances in the estimation of the ERB and, especially, vertical profiles of atmospheric radiative heating in the presence of clouds through improved specification of cloud geometric thickness, identification of multilayer cloud systems, and unique quantitative information concerning vertical variations in cloud microphysical properties. While these benefits come at the cost of reduced spatial coverage relative to most passive instruments such as CERES, the value of accurate cloud vertical structure information is clear when products are analyzed on longer time scales where sufficient statistics can be drawn from the CloudSat data sets. This tradeoff between spatial coverage and vertical resolution is even more pronounced in similar products being developed from Millimeter wavelength Cloud Radar (MMCR) and Micropulse Lidar (MPL) measurements at Atmospheric Radiation Measurement (ARM) Program sites [McFarlane et al., 2007]. While these products offer even greater vertical resolution than CloudSat and provide temporal resolution that is orders of magnitude beyond the capabilities of any conceived constellation of polar orbiting satellites, let alone any single satellite, they yield no spatial coverage beyond the immediate confines of the ARM sites themselves. Thus CloudSat can be thought of as a compromise between satellite-based wide-swath passive cloud sensors and high-resolution ground measurements providing both vertically resolved cloud information as well as the global coverage desired for assessing the impact of clouds on climate.

[5] This paper describes the official level 2 radiative fluxes and heating rates algorithm (2B-FLXHR) and documents properties of the data set over the first year of the CloudSat mission. The theoretical basis of the 2B-FLXHR product and a rough estimate of its accuracy on a variety of space and time scales are provided in sections 2 and 3. An estimate of the global annual radiation budget derived from CloudSat measurements is provided in section 4 while the first full year of 2B-FLXHR data are used to characterize cloud impacts on radiative fluxes at the top of the atmosphere and surface and determine the implied cloud radiative heating in the atmosphere in section 5.

[6] Comparisons of CloudSat observations with visible and infrared radiance measurements from the Moderate Resolution Imaging Spectroradiometer (MODIS) and lidar

observations from the Cloud-Aerosol Lidar and Infrared Pathfinder Satellite Observation (CALIPSO) indicate that thin cirrus, mixed phase clouds, and very shallow or broken stratus clouds may go undetected by CloudSat. Section 6 takes a preliminary look at the anticipated impact of these “difficult clouds” on the 2B-FLXHR product and highlights some potential solutions to this problem that are being explored for future versions of the algorithm.

2. Fluxes and Heating Rates Algorithm

[7] The underlying goal of the 2B-FLXHR algorithm is to produce a vertically resolved radiative flux and heating rate data set that is consistent with observed reflectivities from CloudSat’s CPR. Vertical distributions of liquid and ice cloud effective radii and water contents from the level 2 cloud water content product (2B-CWC) (R. T. Austin and G. L. Stephens, Improved retrieval of stratus cloud microphysical parameters using millimeter-wave radar and visible optical depth: 1. Algorithm and synthetic analysis, submitted to *Journal of Geophysical Research*, 2008; R. T. Austin et al., Improved retrieval of stratus cloud microphysical parameters using millimeter-wave radar and visible optical depth: 2. Application and evaluation, submitted to *Journal of Geophysical Research*, 2008; R. T. Austin et al., Retrievals of ice cloud microphysical parameters using the CloudSat millimeter-wave radar and temperature, submitted to *Journal of Geophysical Research*, 2008) are merged with ancillary temperature and humidity profiles from the European Centre for Medium-Range Weather Forecasts (ECMWF) analyses and surface albedo and emissivity data from the International Geosphere-Biosphere Programme (IGBP) global land surface classification to initialize broadband radiative flux calculations via a two-stream, plane-parallel, doubling-adding radiative transfer model similar to that introduced by Ritter and Geleyn [1992]. The specific model used in 2B-FLXHR employs a delta-Eddington formulation in six shortwave (SW) bands and a constant hemisphere formulation in twelve longwave (LW) bands. In general, Rayleigh scattering, gaseous absorption, and both absorption and scattering by condensed water (liquid and ice) are included. An explicit aerosol model compatible with the algorithm is also available and will be implemented once an ancillary aerosol data set for use with CloudSat has been generated.

[8] The model evaluates fluxes in each spectral band sequentially. Gaseous absorption in each atmospheric layer is first computed using a correlated k formulation [e.g., Lacis and Oinas, 1991; Fu and Liou, 1992]. Cloud optical properties are then assigned to each 240 m vertical range bin that are consistent with the retrieved effective radii and water contents found in CloudSat’s 2B-CWC product using Mie theory for liquid particles and the anomalous diffraction theory-based parameterizations of Stephens et al. [1990] and Mitchell et al. [1996] for ice. In general, the optical properties, τ , ω_0 , and g , vary spectrally but over some of the narrow spectral bands employed in the 2B-FLXHR algorithm these variations are small enough to be neglected. Consequently, while some optical properties must be treated as spectrally variant, others, where possible, are approximated to be grey (invariant within the spectral band) in the interest of computational efficiency.

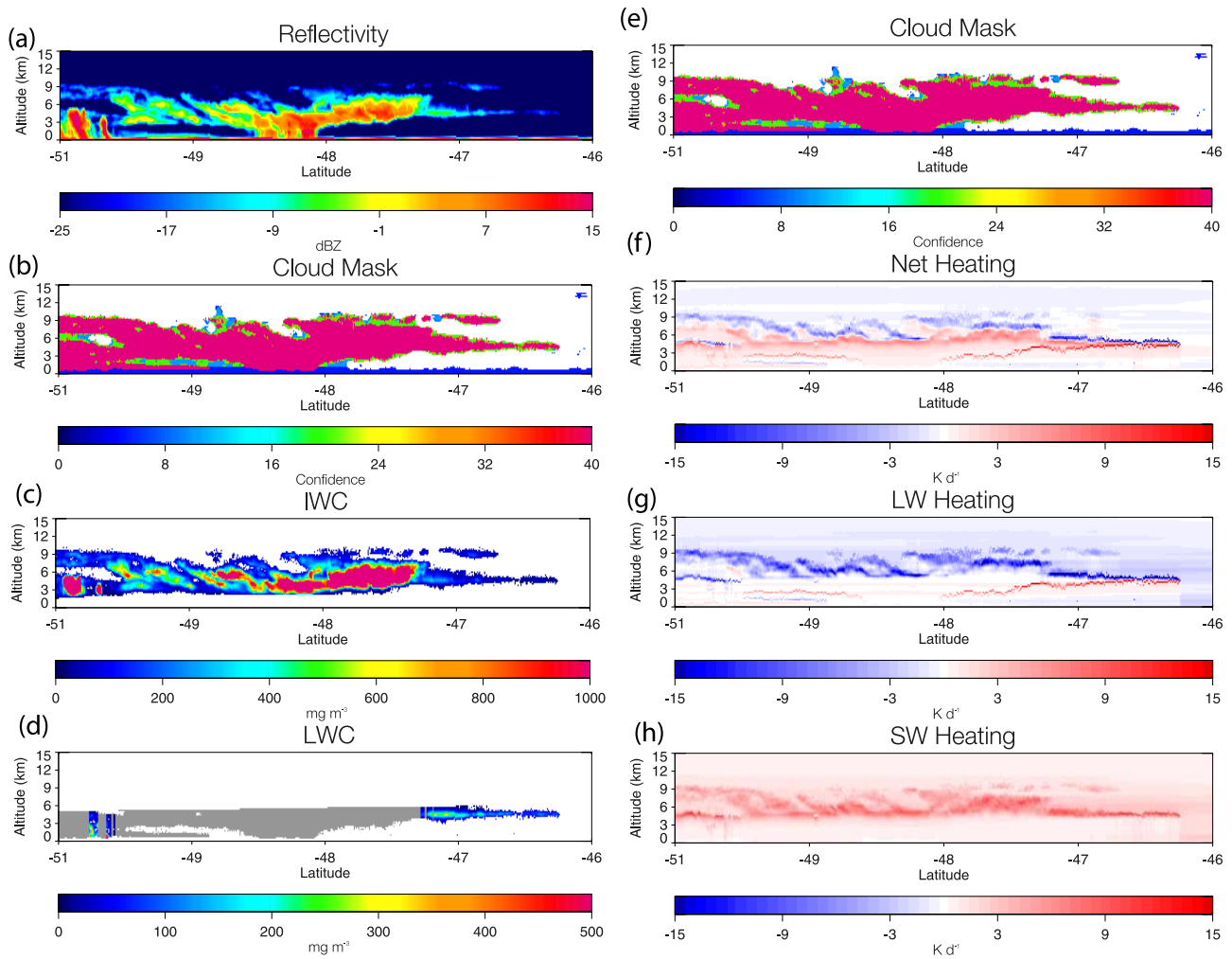


Figure 1. Inputs and outputs from the CloudSat 2B-FLXHR algorithm. (a) Calibrated reflectivity, (b) 2B-GEOPROF cloud mask, (c) IWC, (d) and LWC and (e) cloud mask (repeated), (f) net heating, (g) LW heating, and (h) SW heating (in K d^{-1}). The dark pink shading in Figures 1b and 1e indicates clouds that are detected with high confidence while the green and blue areas denote areas where the cloud signal is less easily distinguished from the background noise. Gray shading in Figure 1d corresponds to regions where clouds are identified but the 2B-CWC quality control flags indicate that the liquid cloud retrieval did not converge to a solution.

[9] When combined with the atmospheric optical properties, these cloud properties describe the reflectance (R), transmission (T), and radiative source (Σ) characteristics of each atmospheric layer that are then combined using the interaction principle, to allow the calculation of the radiative fluxes at the interfaces between them. Computational costs for this adding-doubling form of solution scale linearly with the number of layers [Stephens *et al.*, 2001] making the ~ 100 layer calculations required in 2B-FLXHR tractable. Spectral fluxes from each of the six SW and twelve LW bands are appropriately weighted and combined into the two broadband flux estimates, one over the shortwave from 0 to $4 \mu\text{m}$ and the other over the longwave above $4 \mu\text{m}$. The rate of radiative heating in each layer follows simply by determining the net convergence or divergence of radiative energy into or out of it. The resulting set of SW and LW fluxes and heating rates are output for each CloudSat footprint at the maximum vertical resolution of the CPR and the

2B-CWC product, i.e., 240 m, forming the 2B-FLXHR product.

[10] Several key elements of the 2B-FLXHR algorithm, its inputs, and its primary outputs are summarized for a ~ 500 km orbit segment from 5 November 2006 in Figure 1. Calibrated reflectivity observations from the CPR are shown in Figure 1a followed by the 2B-GEOPROF cloud mask product and corresponding ice water content (IWC) and liquid water content (LWC) retrievals from 2B-CWC. Corresponding heating rates are presented in Figures 1e–1h.

[11] The vertical structure of cloud heating is particularly sensitive to accurate representation of the three regions of multilayer cloudiness in the scene. In addition, the lower ice cloud layer on the right hand side exhibits a wide range in geometric thickness from ~ 1 km south of 46.5°S to more than 6 km around 47.5°S that must be represented to accurately model the downwelling radiation incident at the Earth's surface. Finally, variability in the vertical distribu-

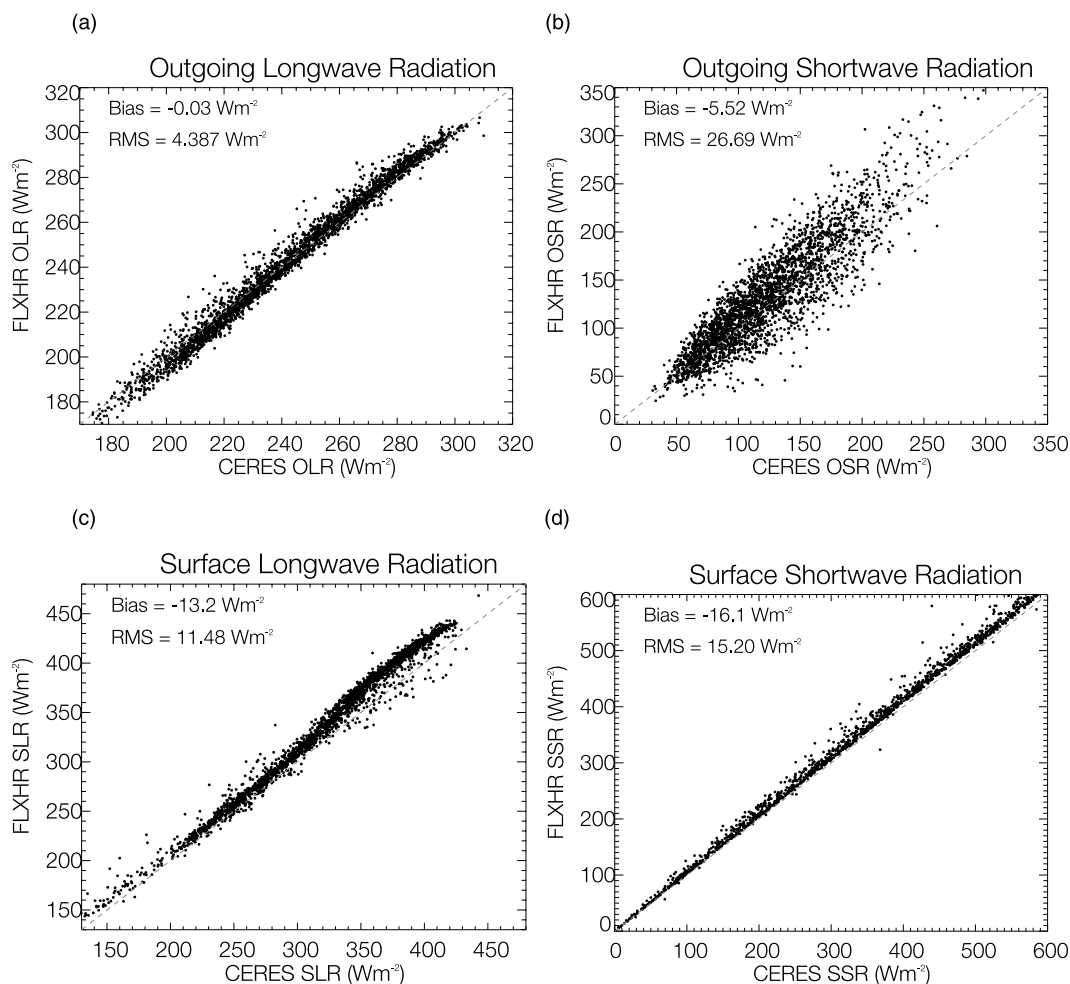


Figure 2. Comparison of monthly, 5° mean TOA and BOA flux estimates from the CloudSat 2B-FLXHR and CERES FLASHFlux products: (a) outgoing LW radiation, (b) outgoing SW radiation, (c) surface LW radiation, and (d) surface SW radiation.

tion of IWC within the cloud itself gives rise to significant vertical structure in the distribution of radiative cooling within the cloud with areas of high IWC typically characterized by narrow regions of strong cooling and areas of lower IWC giving rise to broader areas of weaker cooling.

[12] There are, however, a number of drawbacks to exclusively using CloudSat reflectivity observations to derive radiative flux profiles. The first is the ubiquitous region of ground clutter indicated by the dark blue area in the cloud mask cross section. Here the reflectivity signals in up to four vertical bins above the ground are subject to contamination due to scattering from the side lobes of the transmitted radar pulse potentially obscuring clouds residing in the lowest 1 km of the atmosphere. Another is the fact that very thin cirrus, either isolated or at the tops of thicker systems, can escape detection by CloudSat because of the CPR minimum detectable signal of -30 dBZ. The impacts of each of these types of missing clouds on the accuracy of the 2B-FLXHR product will be assessed using CALIPSO lidar data in section 6. Finally, while CloudSat often provides explicit cloud base information that is not generally available from other sensors, the overwhelming reflectivities observed in precipitation preclude an accurate

assessment of cloud base in rainfall. In addition, it is generally not possible to discriminate between liquid and ice phase hydrometeors in clouds that cross the 0°C freezing level. For consistency with the 2B-CWC product, 2B-FLXHR assumes that the cloud base resides at the lowest level where 2B-CWC reports a nonzero amount of cloud water and adopts the same linear partitioning of liquid and ice water where all layers warmer than 0°C are assumed to contain only liquid and those colder than -20°C are assumed to be ice with a linear transition between these two levels. These assumptions may have significant impacts on the vertical structure of atmospheric heating in the 2B-FLXHR product but less so on the column-integrated heating estimates discussed below.

3. Preliminary Product Evaluation

[13] Despite their different spatial resolutions, coincident estimates of top of the atmosphere (TOA) fluxes from CloudSat and the Clouds and the Earth's Radiant Energy System (CERES) instrument aboard Aqua provide a natural pair of independent data sets that can be compared to yield a first-order estimate of their uncertainties over a wide range

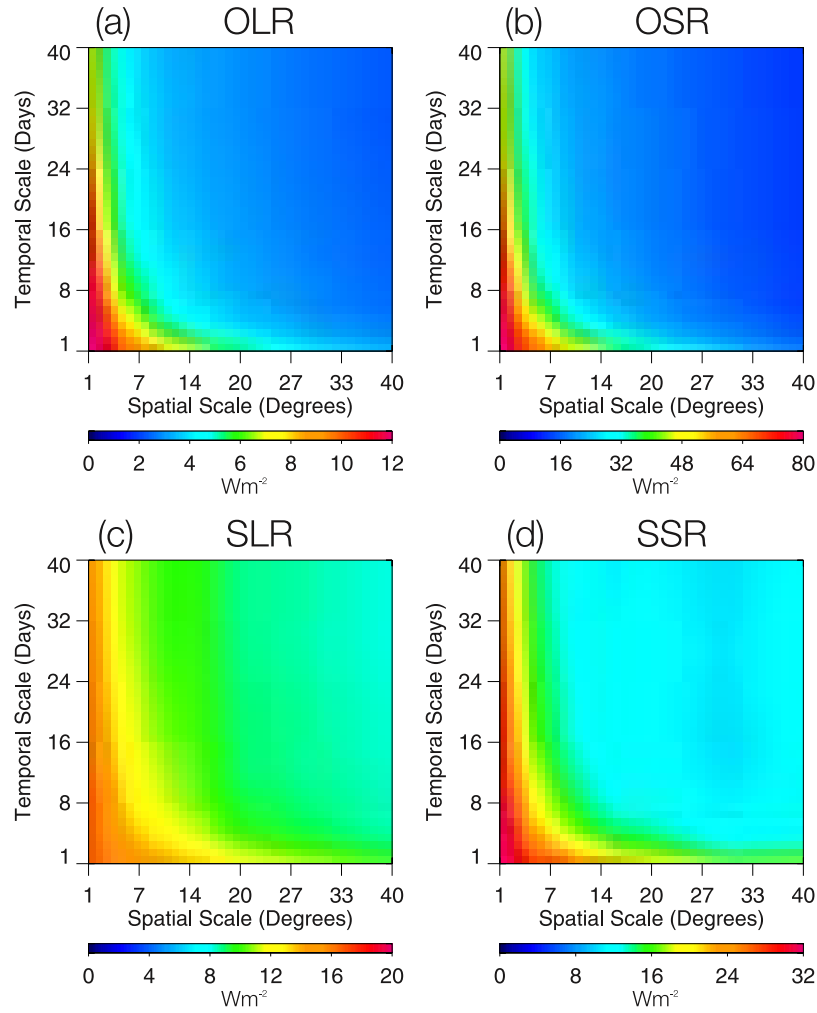


Figure 3. RMS differences between TOA and BOA flux estimates from 2B-FLXHR and the CERES FLASHFlux product on a variety of time and space scales.

of different cloud scenes, surface types, and environmental conditions. Neither the 2B-FLXHR nor the algorithm used to produce the CERES FLASHFlux product [Stackhouse *et al.*, 2006] analyzed here have been tuned to agree with one another under any conditions, so the differences between their flux estimates provide a useful metric for measuring the combined uncertainties in these products. Furthermore, CloudSat’s vertically resolved cloud profiles are particularly difficult to evaluate on a global scale given the lack of similar measurements from another platform. However since these products ultimately drive the calculation of fluxes and heating rates in 2B-FLXHR, comparisons against the CERES FLASHFlux product can be thought of as providing a first global evaluation of the entire CloudSat algorithm stream since uncertainties at any stage in the processing stream propagate into downstream products.

[14] A sample comparison of CloudSat and CERES flux estimates accumulated into 5° , monthly bins is presented in Figure 2. Two months of data are considered and each CloudSat granule has been rigorously matched to the corresponding CERES swath to isolate the closest CERES field of view to each individual CloudSat pixel. Each data point in Figure 2 represents the average of all data from both

instruments that fall into any given 5° box at any time during the month. Also included on Figure 2 are the RMS difference between the two products and their bias over the full 2 month data set. No additional subsetting of the data has been conducted in this analysis so some amount of scatter is inevitable because of sampling mismatches between the CloudSat and the CERES 10 km footprint.

[15] RMS differences between CERES and CloudSat estimates of outgoing longwave radiation (OLR) are less than 5 W m^{-2} while those in the OSR exceed 26 W m^{-2} . It is encouraging to note that these uncertainties are, to a large extent, random on the global scale as evidenced by the fact that they average out to yield a bias of less than 1 and 6 W m^{-2} , respectively.

[16] The ultimate uses of many global products like 2B-FLXHR are likely to span a wide range of space and time scales ranging from those characteristic of individual cloud systems up to the large region/monthly scales required to study climate processes. It is, therefore, important to assess the accuracies of such products on a variety of space-time averaging scales to provide uncertainty estimates that appropriately account for the relative importance of random and systematic errors. To these ends, Figure 3 presents RMS

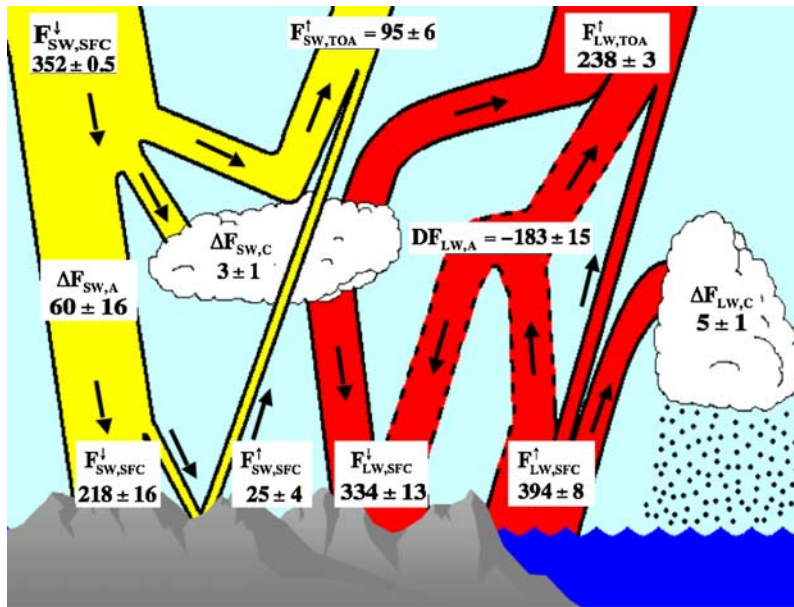


Figure 4. Annual mean Earth’s radiation budget from 82°N to 82°S from the full year of CloudSat observations between September 2006 and August 2007. Contributions to atmospheric radiative heating from clear skies are represented by $\Delta F_{SW/LW,A}$, and those due to clouds are represented by $\Delta F_{SW/LW,C}$. Quoted uncertainties represent the difference between the 2B-FLXHR product and TOA and SFC flux estimates from the CERES FLASHFlux product combined with estimates of uncertainties in the prescribed surface emissivity and albedo. Errors in derived estimates of atmospheric flux convergence represent combinations of the uncertainties in the fluxes used to derive them.

differences between estimates of TOA and BOA fluxes from matched CloudSat and CERES products over spatial scales ranging from 1 to 40° and temporal scales from 1 to 50 days.

[17] At spatial scales less than about 5°, the impacts of CloudSat’s nadir sampling are evident in the fact that RMS differences remain large even when averaging over significant time scales. At 1° resolution, for example, it takes up to 16 days for a return pass from CloudSat in the same grid box and even averaging over 50 days reduces errors by less than a factor of two. Sampling improves dramatically, however, at spatial scales larger than 10° resulting in a dramatic reduction in the RMS differences between CloudSat and CERES, particularly when data is further aggregated to 5 day temporal resolution or longer.

[18] Also evident from Figure 3 is the asymptotic nature of the RMS differences implying that uncertainties at longer space/time scales are ultimately dominated by biases between the products that cannot be reduced by additional averaging. The residual bias in OLR after globally averaging 2 months of data is 2 W m⁻² although this excellent agreement should not be taken as proof that either of the products are really accurate to this level since, for example, both CERES and CloudSat fly in a similar Sun-synchronous orbit and neither instrument samples the diurnal cycle. Biases in OSR, SLR, and SSR are -5.5 W m⁻², -13 W m⁻², and -16 W m⁻², respectively. Given the tenuous nature of specifying cloud base using passive observations and the challenges associated with extracting low cloud information from the clutter region in the CloudSat observations (see below), it is not surprising that the biases in surface

fluxes are much larger than those at the top of the atmosphere.

4. Earth’s Radiation Budget Based on the First Year of CloudSat Data

[19] The radiative fluxes and heating rates algorithm has been applied to all CloudSat data starting on 15 June 2006 the first official day of regular radar observations. Here we examine the “Release 4” (R04) 2B-FLXHR data set from September 2006 through August 2007. Perhaps the most recognizable representation of this “first year” of data is through the ERB diagram shown in Figure 4. Area-weighted LW and SW fluxes at the top of the atmosphere (TOA) over the complete latitude range sampled by CloudSat (82°N/S) are presented along with estimates of the atmospheric radiative heating and cooling and that due to clouds, denoted by $\Delta F_{SW/LW,A}$ and $\Delta F_{SW/LW,C}$, respectively. SW flux estimates have been normalized, on a pixel-by-pixel basis, using appropriate diurnally averaged incoming SW radiation at the latitude, day, and local time of each observation in an effort to crudely remove the effects of the diurnal cycle of solar insolation. In principle such a rescaling requires performing alternate radiative transfer calculations at different times of day and average the results to more accurately represent the dependence of albedo on solar zenith angle but this is not practical given the enormous volume of the 2B-FLXHR data set.

[20] The TOA flux estimates in Figure 4 provide a natural, first-order consistency check on the 2B-FLXHR product allowing us to determine how close these products come to closing the Earth’s radiation budget. Combining the

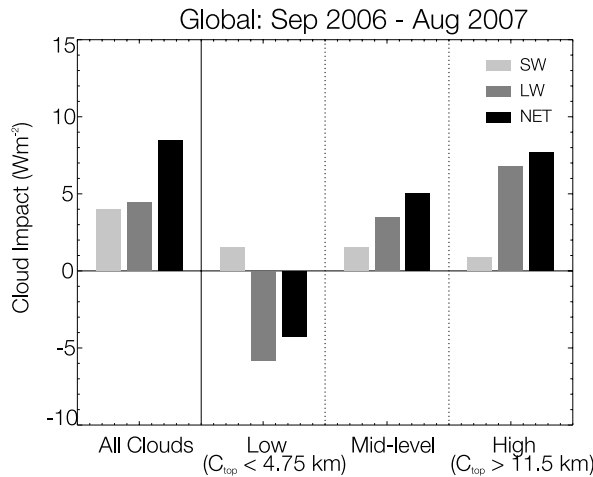


Figure 5. Global and annual mean cloud impacts on atmospheric radiative heating and its breakdown into high-, middle-, and low-topped cloud pixels.

relevant fluxes, the TOA energy budget balances to within a relatively small surplus of $\sim 19 \text{ W m}^{-2}$. Given the characteristics of CloudSat's sampling, namely, its Sun-synchronous orbit that samples at only two distinct times throughout the diurnal cycle, it is unreasonable to expect perfect closure of the global ERB. Furthermore, the lack of a swath constrains the CloudSat observations to lie between $\pm 82^\circ$ introducing a slight low-latitude bias in the product, that would be expected to result in a surplus of radiation into the region. This is evidenced by the fact that the average incoming SW radiation in this region is 10 W m^{-2} larger than the global value of 342 W m^{-2} and likely leads to an underestimate in the planetary albedo by undersampling bright ice surfaces in polar regions relative to darker tropical oceanic regions. Conversely, similar arguments suggest that outgoing long-wave radiation (OLR) is likely overestimated for the same reasons but it is impossible to know the extent to which these two effects cancel. On the basis of the uncertainty analysis below, it is anticipated that most of the uncertainty that cannot be explained by sampling effects is likely accounted for by errors in outgoing SW radiation (OSR) due to low clouds that are missed by CloudSat.

[21] In general, the LW fluxes from CloudSat agree very well with those from prior studies such as those of Hartmann [1994], Kiehl and Trenberth [1997] and Liou [2002] that span ranges of $235\text{--}240 \text{ W m}^{-2}$ in OLR and $376\text{--}390 \text{ W m}^{-2}$ in surface emitted LW radiation. Combining these quantities with the emitted LW radiation from the atmosphere to the surface, the resulting atmospheric radiative cooling of 178 W m^{-2} predicted by 2B-FLXHR easily agrees with the $167\text{--}173 \text{ W m}^{-2}$ to within the stated

measurement uncertainties. Estimates of atmospheric SW radiative heating in the literature span a much wider range owing to discrepancies in the total downwelling SW radiation that reaches the surface. Again the CloudSat estimate of 63 W m^{-2} falls within the $58\text{--}78 \text{ W m}^{-2}$ of the aforementioned studies. The reflected SW radiation by the atmosphere, clouds, and surface, however, is underestimated in the current study with respect to the $103\text{--}107 \text{ W m}^{-2}$ range in these prior studies consistent with an underrepresentation of low clouds in the 2B-CWC product.

[22] Vertical structure information provided by CloudSat also makes it possible to quantify cloud contributions to atmospheric radiative heating that require cloud base information not readily available from passive sensors. It is evident from Figure 4 that the vast majority of atmospheric heating comes from clear skies while the global mean cloud contributions, represented the Δ terms, is on the same order of magnitude as the uncertainties in most fluxes. This is explained, in part, by Figure 5 where global cloud radiative heating is broken down into contributions from low-, middle-, and high-topped cloud pixels defined as CloudSat pixels where the upper most cloudy layer lies below 4.75 km, between 4.75 and 11.5 km, and above 11.5 km, respectively. This simple and admittedly somewhat arbitrary classification illustrates that the small net impact of clouds globally owes its origins, at least in part, to a cancellation between the cooling effects of low clouds and the heating from high-topped clouds.

5. Impact of Clouds on Radiative Heating in the 2B-FLXHR Data Set

[23] Globally averaged cloud impacts on TOA and Bottom of the Atmosphere (BOA) (or surface) radiative fluxes, defined as the difference in net flux between clear-sky and all-sky conditions, $C = (F_{up} - F_{dn})_{clear-sky} - (F_{up} - F_{dn})_{all-sky}$, are reported in Table 1. On the annual mean, clouds result in a net radiative cooling of 18.6 W m^{-2} , reflecting 40.2 W m^{-2} more SW radiation to space than in clear skies while trapping an additional 21.6 W m^{-2} in the LW, remarkably consistent with estimates from the Earth's Radiation Budget Experiment (ERBE) reported nearly two decades ago by Harrison *et al.* [1990]. Using the explicitly resolved cloud base information provided by CloudSat, the 2B-FLXHR data set indicates that all of this cooling manifests itself at the Earth's surface while clouds actually impart a small net warming to the atmosphere.

[24] While the net impact of clouds on the global atmospheric heating is rather small, they exhibit significant impacts on regional scales that directly influence large-scale circulation patterns by modulating local energy gradients [Sohn and Smith, 1992c; Slingo and Slingo, 1988, 1991;

Table 1. Globally Averaged Cloud Radiative Impacts on TOA and BOA Radiative Flux Estimates Defined as $F_{clear} - F_{allsky}$ ^a

Flux	All Clouds	$C_{top} < 4.75 \text{ km}$	$4.75 < C_{top} < 11.5 \text{ km}$	$C_{top} > 11.5 \text{ km}$
$F_{up,TOA}^{TOA}$	21.6	2.5	12.3	6.8
$F_{up,BOA}^{BOA}$	-40.2	-9.4	-21.5	-9.2
$F_{dn,SW}^{SW}$	-16.7	-6.5	-9.0	-1.3
$F_{dn,LW}^{LW}$	43.3	10.2	23.2	9.9

^aUnit is W m^{-2} . The first column represents all clouds while the others indicate the contributions of the low-, middle-, and high-topped cloud pixel categories defined in section 4.

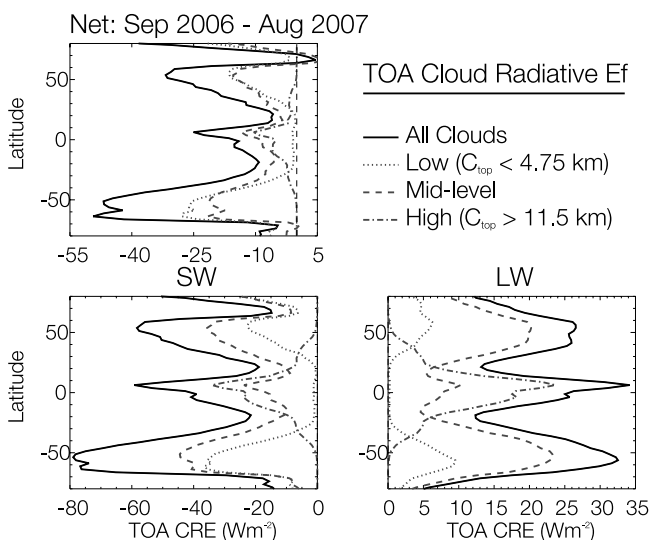


Figure 6. Zonally averaged cloud impacts on outgoing TOA radiative fluxes for the same period as in Figure 4. The black curve represents the total from all clouds while the dotted, dashed, and dot-dashed curves show its breakdown into contributions from low-, middle-, and high-topped cloud pixels, respectively.

[L'Ecuyer and Stephens, 2003]. Figure 6 extends the analysis to examine the contributions of each cloud type to zonally averaged TOA cloud radiative effects (CRE). Cloud LW effects peak in the tropics at 35 W m^{-2} , drop to about a third of this value in the descending branches of the Hadley circulation at around $\pm 20^\circ$, and increase again to $26\text{--}32 \text{ W m}^{-2}$ in the higher-latitude storm tracks. For the 2006–2007 period analyzed, there is an asymmetry at higher latitudes where cloud effects tend to be larger in the Southern Hemisphere than at equivalent latitudes in the north. SW cloud radiative impacts are uniformly larger than those in the LW with the exception of a small region from $60\text{--}70^\circ\text{N}$ where net cloud effects are slightly tilted in favor of LW heating. Zonal variations in SW cloud impacts tend to mirror those in the LW although the SW peaks in the higher-latitude storm tracks tend to be larger than those in the tropics and the asymmetry between the Northern and Southern Hemispheres is more pronounced. This is likely a result of the fact that clouds in the Southern Hemisphere are more likely to reside over the ocean providing a stronger albedo contrast relative to clear-sky conditions. These results are also qualitatively consistent with those shown in previous work [e.g., Harrison *et al.*, 1990; Hartmann *et al.*, 1992] and the overall magnitudes of the variations are very similar.

[25] Not surprisingly, high clouds provide the dominant LW cloud radiative impacts in the tropics and their effects systematically decrease, vanishing at the poles where the low- and middle-topped clouds dominate. Clouds in the intermediate category tend to exhibit significant contributions at all latitudes since only mid-topped cloud pixels are observed in substantial quantities at all latitudes (Figure 7). This does not mean that low clouds do not exist in the tropics but such clouds are generally accompanied by overlying cirrus and are therefore masked when cloud top

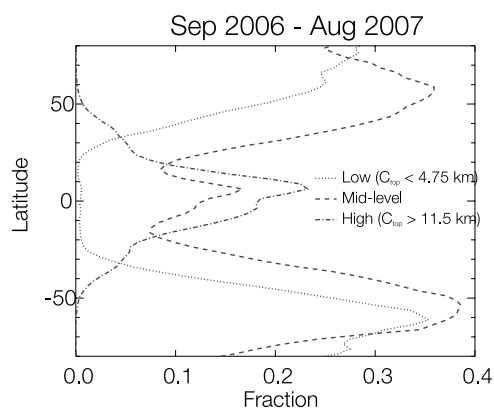


Figure 7. Fraction of observations in each latitude band where the highest cloud pixel fell into the low (dotted), middle (dashed), and high (dot-dashed) categories during the full year period from September 2006 through August 2007.

is used to categorize each CloudSat pixel. In the SW the impacts of clouds in this intermediate category are even more pronounced, comparable to those from high clouds in the tropics and those from low clouds in polar regions. It is also evident that the SW radiative effects of middle- and low-topped clouds in the storm tracks are larger than those due to tropical cirrus leading to the stronger cooling peak at higher latitudes.

[26] While TOA radiative fluxes control net radiative forcing on the climate system, estimating atmospheric radiative heating requires knowledge of surface radiation as well. Zonally averaged BOA CRE are summarized in Figure 8 providing the key information required to understand the impacts of clouds on atmospheric radiative heating. For example, the large amount of water vapor present in tropical regions, leads to a pronounced minimum in long-wave BOA CRE between $\pm 30^\circ$ where high-topped clouds that have significant impacts on TOA LW fluxes dominate.

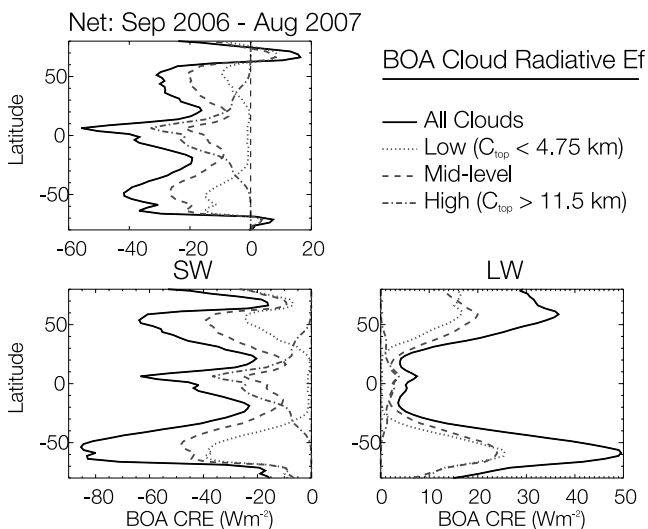


Figure 8. As in Figure 6 but for downwelling radiative fluxes at the BOA.

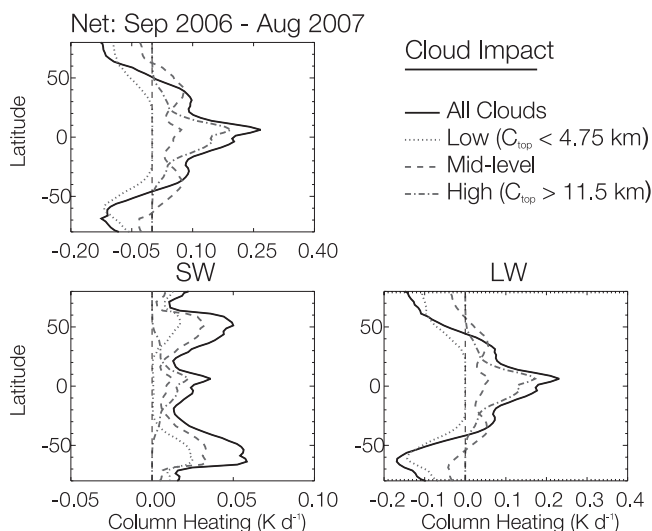


Figure 9. Cloud impacts on atmospheric radiative heating (expressed in K d^{-1}) given by the difference between the cloud impacts at TOA and BOA shown in Figures 6 and 8, respectively.

At higher latitudes where sea surface temperatures are colder and atmospheric water vapor is reduced, BOA LW CRE increases to much larger values in the storm tracks where clouds with lower tops and, therefore, smaller TOA impacts tend to dominate. Cloud effects on SW fluxes at the surface, on the other hand, are only slightly smaller than those at TOA and exhibit almost identical variations with latitude. Thus, as a result of the strong tendency for high-topped clouds to exist in regions of high water vapor, the opposing LW impacts of high- and low-topped clouds represent the only appreciable source of changes in atmospheric radiative flux convergence.

[27] The zonally averaged contribution of clouds to atmospheric LW, SW, and NET radiative heating, defined as the difference between TOA and BOA cloud radiative impacts from Figures 6 and 8, $\Delta F_{cloud} = CRE_{TOA} - CRE_{BOA}$, is shown in Figure 9 expressed in units of K d^{-1} . Although clouds exert the largest impacts on SW fluxes, SW cloud heating is generally weak because of the near cancelation of TOA and BOA cloud radiative effects. As a result, cloud impacts on LW fluxes dominate zonal variations in net heating. High-topped cloud pixels in the tropics trap significantly more OLR than can be emitted back to the surface in the presence of high ambient water vapor concentrations leading to a net cloud heating of $\sim 0.2 \text{ K d}^{-1}$. At higher latitudes, on the other hand, low-topped clouds significantly increase the LW radiation emitted from the atmosphere to the surface resulting in a net atmospheric radiative cooling of more than 0.15 K d^{-1} . While the intermediate cloud category has significant impacts on TOA and BOA fluxes, these effects largely cancel and, despite their significant concentrations at all latitudes, they play very little role in determining the observed zonal variations of cloud heating. This is consistent with Table 1 where it is clear that, in a globally mean sense, of all the TOA/BOA flux impact pairs only the LW radiative effects of high and low cloud top scenes are significantly different

between TOA and BOA. Finally, the fact that the contributions from the individual cloud types may be larger than the global impacts they sum to supports the assertion of *Chen et al.* [2000] that even a small shift in the relative frequency of occurrence of the different cloud types in a region may significantly impact its radiation budget even if total cloud cover remains constant.

6. Role of “Difficult Clouds”

[28] As noted above there are some clouds for which the current version of 2B-FLXHR, that relies exclusively on CloudSat observations, suffers from either an inherent lack of radar sensitivity or the presence of ground clutter. Examples of these “difficult clouds” are presented in Figure 10 where cloud masks from the 2B-GEOPROF and 2B-GEOPROF-LIDAR, an analogous product based on cloud returns from both CloudSat and CALIPSO, are compared. Careful examination of Figure 10f illustrates the three main types of clouds that pose problems for the 2B-FLXHR algorithm in the absence of ancillary data. The first type, indicated by the 1 on Figure 10f, is thin cirrus that falls below the minimum detectable signal of the CPR. At 2 an example of low cloud obscured by ground clutter is evident while 3 indicates a region of precipitation where the CloudSat LWC algorithm does not converge as indicated by the masked out region in Figures 10d and 10h. Also shown is an example of a mixed phase cloud (indicated by 4), that not only poses a challenge to CloudSat but whose properties are also difficult to constrain using ancillary VIS/IR and lidar information because of the simultaneous presence of both liquid and ice in the same vertical bin. In this case the undetected portion of the cloud on the left is likely composed primarily of small liquid cloud drops while portions of the cloud further to the right likely contain more numerous ice crystals that are larger and easier to detect. In both cases it is difficult to determine the precise ratio of liquid to ice water content introducing potential uncertainty in simulated fluxes.

6.1. Undetected Clouds

[29] To roughly quantify the impacts of thin cirrus and obscured low clouds (cases 1 and 2 in Figure 10) on the accuracy of the 2B-FLXHR flux estimates, approximate estimates of their mean properties were made using a combination of in situ observations from past field campaigns, direct comparisons between CloudSat and CALIPSO observations and equivalent comparisons of ground-based high spectral resolution lidar and mm-wavelength radar. On the basis of the combination of the minimum detectable LWC as observed in the CloudSat’s 2B-CWC product and the liquid cloud climatology of *Miles et al.* [2000], low-level clouds that are detected by CALIPSO but not CloudSat are assumed to have an effective radius of $9 \mu\text{m}$ and an average LWP of 50 mgm^{-3} yielding a visible optical depth of ~ 7 for a 1 km thick cloud. Ice cloud properties are determined from CALIOP observations wherever a cloud is observed by CALIPSO but not by CloudSat. Aspects of the retrieval procedure, that is based on the lidar transmission method [e.g., *Comstock and Sassen, 2001; Lo et al., 2006*] are illustrated in Figure 11. The closest total attenuated backscatter profile from CALIPSO’s CAL_LID_L1-Prov-V1-10

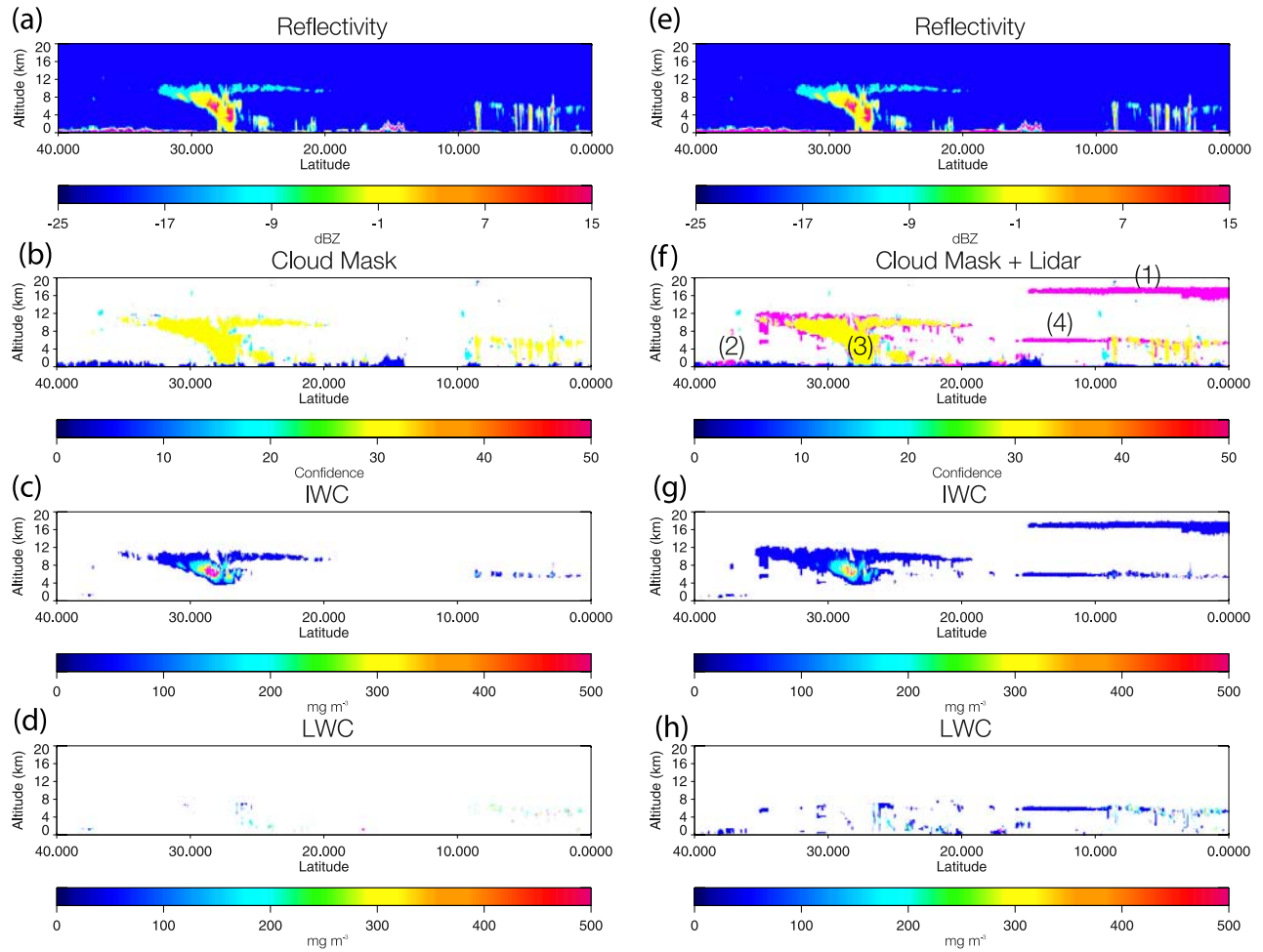


Figure 10. Example of “difficult clouds” from the perspectives of CloudSat and CALIPSO. (a–d) CloudSat observations, radar-only cloud mask, and liquid and ice water contents and (e–h) additional clouds revealed by CALIPSO. In this case, clouds detected with high probability using CloudSat measurements are shown in orange while clouds that are observed by CALIPSO but not CloudSat appear in dark pink in Figures 10b and 10f.

product to each CloudSat footprint is identified and the nearest 15 points are averaged to create a 5 km mean profile with reasonable signal to noise characteristics. Pressure and temperature profiles from ECMWF are interpolated to the lidar altitude grid in order to create a profile of Rayleigh backscatter, represented by the red line in Figure 11. As seen in Figure 11, above the cloud layer the predicted Rayleigh backscatter approximately matches the measured backscatter. Below the cloud, however, the measured backscatter is less than the calculated Rayleigh backscatter due to extinction from the cloud layer. Using simple exponential fits to both the Rayleigh backscatter and measured backscatter below cloud in the form of $\beta = Ae^{-z/H}$, the ratio of the coefficients, $A_{Measured}/A_{Rayleigh} = e^{-2\tau_{cld}}$, yields an estimate of the cloud optical depth, τ_{cld} . Because of the increased noise characteristics of daytime CALIOP backscatter observations, this analysis is restricted to nighttime profiles for the purposes of the present study.

[30] Figure 12a shows the mean extinction for all lidar-only clouds as a function of mean cloud temperature for the months of June, July, and August 2007. For comparison, an equivalent relationship derived from colocated Advanced

High Spectral Resolution Lidar (AHRSL) and Millimeter-wave Cloud Radar (MMCR) products from Eureka, Canada ($\sim 82^\circ\text{N}$, 86°W) for the same period is shown in Figure 12c (data courtesy of the University of Wisconsin Lidar Group (<http://lidar.ssec.wisc.edu/>)). Cloud properties are accumulated for all scenes in which the AHRSL observed a cloud whose MMCR reflectivity fell below the -30 dBZ minimum detectable signal (MDS) of the CPR. The results suggest that the average extinction of a cloud that is detected by the lidar but not the radar is generally less than 0.1 km^{-1} with the exception of clouds warmer than 245 K that may contain supercooled liquid water. Corresponding cloud extinction estimates from Eureka are summarized in Figures 12c and 12d to provide a crude consistency check on the satellite results. While agreement between the ground and satellite-based results is reasonably good at warmer temperatures the two data sets exhibit opposite temperature dependencies leading to significant discrepancies at colder temperatures where the extinction estimates from Eureka are as much as a factor of 3 larger than those from the satellites. These discrepancies likely stem from the dramatically different origins of the samples used in each case and,

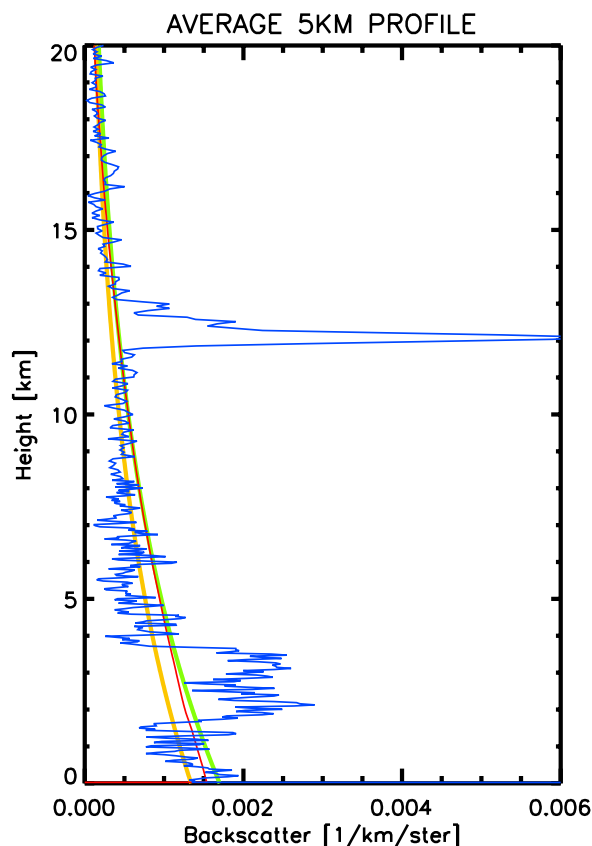


Figure 11. Example of a molecular backscatter profile from CALIPSO for a cloud that was not observed by CloudSat. The blue curve traces the observed backscatter while the other three lines represent the expected Rayleigh backscatter in the absence of cloud (red curve), an exponential fit to this line (green curve), and the measured molecular backscatter below cloud (yellow curve).

in particular, the fact that the colder clouds missed by CloudSat in the tropics are likely to be much more heavily weighted toward high, thin, subvisual cirrus than those missed by the MMCR at Eureka. This is supported by similar analyses conducted by *Comstock et al.* [2002] that suggest that clouds escaping detection by the MMCR at the tropical Nauru site typically had optical depths less than 0.1.

[31] For application in the 2B-FLXHR framework, these cloud extinction estimates were converted to IWC by assuming an ice crystal effective radius and noting that the scattering properties of small ice crystals satisfy the Rayleigh approximation at the wavelength of the CPR. The open circles, solid circles, and open square symbols depicted in Figures 12b and 12d indicate equivalent IWC as a function of temperature for effective radii of 20, 30, and 40 μm , respectively. On the basis of climatological observations and considerations of the MDS of the CPR, an effective radius of 30 μm is adopted for all thin cirrus clouds missed by CloudSat in the current study allowing optical properties to be estimated for the remaining 17 spectral bands in the broadband radiative transfer calculations. For simplicity, the IWC is assumed to be 1.5 mgm^{-3} independent of cloud temperature. This is consistent with the largest

mean IWC of the lidar-only clouds colder than 245 K when an effective radius of 30 μm is assumed. On the basis of the comparison with Eureka data it is recognized that a more sophisticated pixel-by-pixel approach will ultimately be needed to accurately represent missing clouds in specific scenes but it is anticipated that the more simplistic approach outlined here will yield a reasonable estimate of the impacts of these clouds in a statistical sense.

[32] An experimental version of the 2B-FLXHR algorithm that incorporates these cloud properties according to the 2B-GEOPROF-LIDAR product in addition to the standard 2B-CWC clouds was applied to 6 months of CloudSat and CALIPSO data from December, January, and February 2006–2007 and June–August 2007 to quantify the uncertainties in 2B-FLXHR due to these “difficult clouds.” Because of the statistical nature of the estimated cloud properties, the resulting fluxes will not necessarily be representative of any individual cloud system but are designed to provide a meaningful estimate of their average effect on large-scale average flux estimates. It is also worth noting that the IWC is purposely chosen to be larger than the mean at almost all temperatures so that the resulting error estimates will provide upper bounds on the true global impacts of these clouds. At an altitude of 18 km, for example, the IWC of the thin cirrus cloud depicted in Figure 10 is likely decidedly less than 1.5 mgm^{-3} as indicated by Microwave Limb Sounder (MLS) observations that suggest that the typical IWC of clouds at this altitude is closer to 0.05 mgm^{-3} [*Wu et al.*, 2008].

[33] The mean differences between the modified and standard 2B-FLXHR algorithm products for the 6 months analyzed are summarized in Table 2. The impacts of undetectable high and low clouds are reported separately using 2B-GEOPROF-LIDAR to discriminate between them. Undetected thin cirrus exert the largest impact on the outgoing longwave radiation where they trap 2.5 W m^{-2} more radiation than the radar-only clouds alone. This error is within the spread in globally averaged OLR estimates from prior studies. Low clouds have a considerably larger influence, particularly on shortwave fluxes. With the assumptions outlined above, the omission of low clouds that go undetected by CloudSat can lead to an underestimate of almost 20 W m^{-2} in the total reflected SW radiation and an even larger overestimate of the shortwave flux that reaches the surface because of absorption, consistent with prior studies [*Miller and Stephens*, 2001; *Stephens et al.*, 2002; G. G. Mace et al., A description of hydrometeor layer occurrence statistics derived from the first year of merged CloudSat and CALIPSO data, submitted to *Journal of Geophysical Research*, 2008].

[34] Additional insights into the location and impacts of thin high clouds and undetected low clouds can be gleaned from Figure 13 where global maps of the monthly mean difference between the modified and standard radar-only versions of 2B-FLXHR at 5° resolution are presented. OLR differences are localized in three tropical regions where high thin clouds are commonly found associated with moisture transported into the upper troposphere by frequent intense deep convection. Outside these regions the impacts of thin high clouds that are not detected by CloudSat are generally much smaller, often less than 2 W m^{-2} . Differences in OSR suggest that low clouds that are obscured by ground clutter

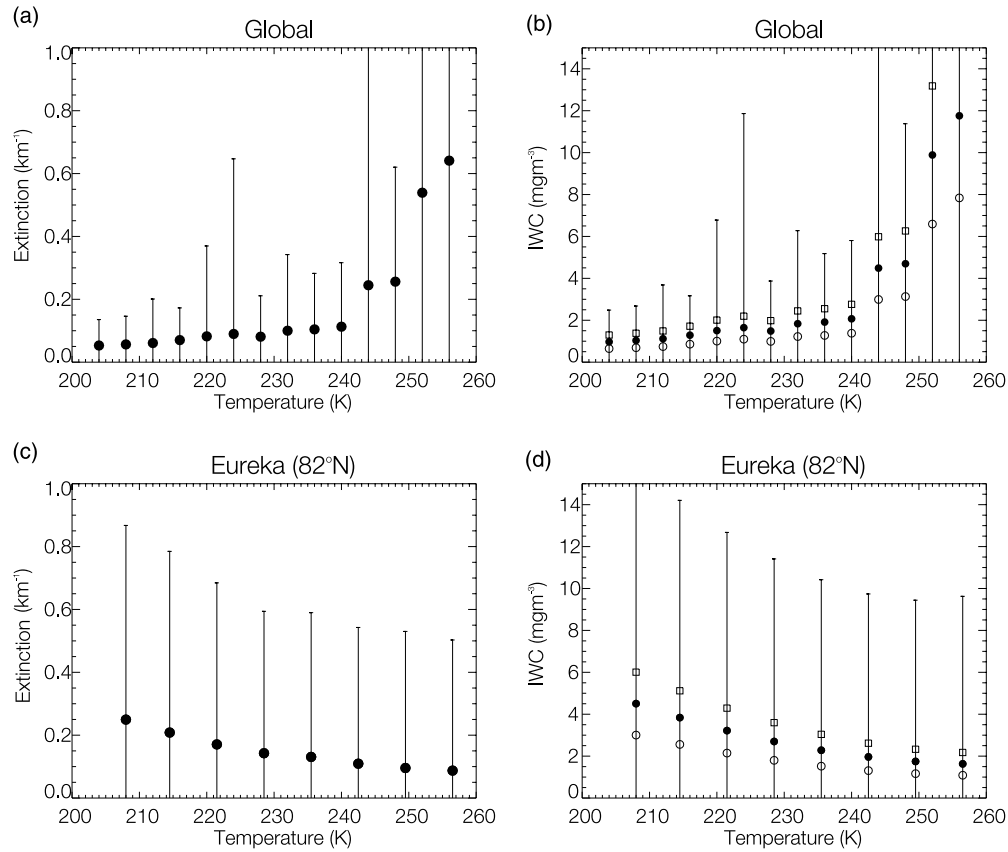


Figure 12. High cloud properties derived from colocated radar and lidar observations. (a) Global mean extinction and (b) IWC of clouds observed by CALIPSO but not CloudSat. (c and d) Analogous cloud properties derived by matching ground-based MMCR and AHSRL measurements at Eureka, Canada. In Figures 12b and 12d, solid circles correspond to an effective radius of 30 μm while open squares and open circles correspond to 40 and 20 μm , respectively.

in the CloudSat observations are much more widespread although larger errors are evident in the marine stratocumulus regions off the west coasts of North and South America and in the region of persistent low clouds and fog in the South American rain forest. Surprisingly, the errors in SW fluxes due to undetected low clouds are larger than the biases between CloudSat and CERES. This suggests that there may be other uncertainties in the 2B-FLXHR algorithm that partially compensate for the missing clouds. Uncertainties in retrieved cloud properties, the prescribed partitioning of condensed water into liquid and ice phases in mixed phase regions of clouds, subpixel variability within the CloudSat footprint, uncertainties in cloud base, and errors in ECMWF temperature and humidity profiles may all introduce uncertainty in the 2B-FLXHR product that require further investigation through more detailed field experiments that are currently underway.

6.2. Precipitation

[35] Drizzling and especially precipitating clouds (case 3 in Figure 10) also pose a challenge to the 2B-FLXHR algorithm since they often cause the antecedent 2B-CWC liquid water content retrievals to fail because of the large reflectivities encountered in the presence of large droplets (Austin and Stephens, submitted manuscript, 2008). At present, 2B-CWC identifies all retrievals that are potentially

contaminated by precipitation using a reflectivity threshold of -15 dBZ. Whenever the liquid water content retrieval fails under these conditions the 2B-FLXHR algorithm assumes that precipitation is present and that the associated cloud is optically opaque. All radar bins that meet the required reflectivity threshold are assigned a LWC of 0.5 gm^{-3} consistent with the largest LWCs that are reliably retrieved with the 2B-CWC algorithm and the algorithm proceeds as described in section 2. Uncertainties due to this assumption are evaluated through an additional set of sensitivity studies in which the assumed threshold LWC is first doubled and then halved. Global mean differences in TOA and BOA upwelling and downwelling fluxes between

Table 2. Globally Averaged Impacts of “Difficult Clouds” on TOA and BOA Radiative Flux Estimates^a

Cloud Type	$\Delta F_{up,SW}^{TOA}$	$\Delta F_{dn,SW}^{SFC}$	$\Delta F_{up,LW}^{TOA}$	$\Delta F_{dn,LW}^{SFC}$
Thin high clouds	1.0	-1.2	-2.5	1.9
Obscured low clouds	19.5	-24.4	-1.7	14.5
Precipitation	6.9	-8.1	-0.07	0.05

^aUnit is W m^{-2} . In the case of thin high and low clouds, differences correspond to the modified 2B-FLXHR algorithm – the original. For the precipitation case, differences between the double LWC and half LWC cases are reported.

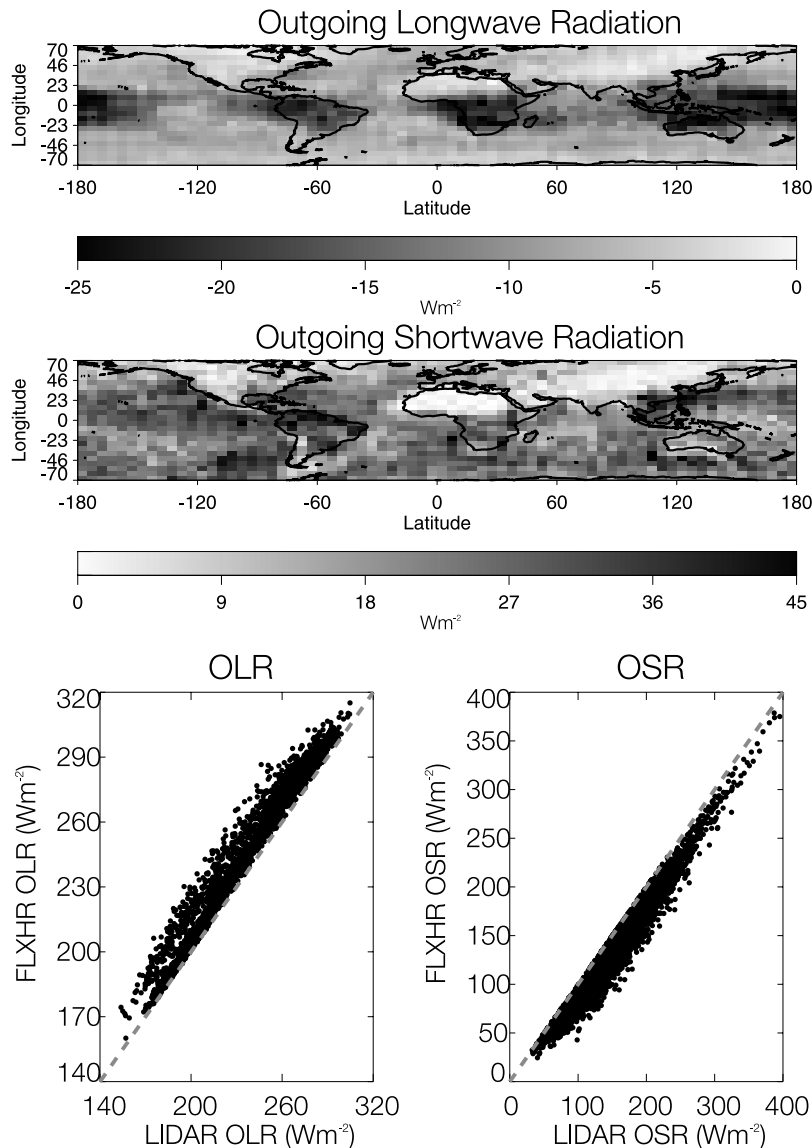


Figure 13. Global distributions of the impacts of undetected high and low clouds on CloudSat's TOA radiative flux estimates. (top) Maps of monthly mean OLR and OSR differences between the CloudSat + CALIPSO algorithm and the standard 2B-FLXHR algorithm at 5° resolution and (bottom) these data cast in the form of scatter diagrams.

these two extreme cases are also summarized in Table 2. Errors due to the ill-defined LWC in precipitation exclusively impact the albedo of precipitating clouds, in particular those in which warm rain processes dominate, amounting to errors of $7\text{--}8\text{ W m}^{-2}$ in shortwave fluxes, significantly less than those introduced by missing low clouds. This is, in part, due to the fact that precipitating scenes account for less than 15% of the CloudSat observations but more so to the fact that the clouds in these scenes are generally so optically thick that their albedos and emissivities are effectively saturated and no longer vary with LWC.

7. Summary

[36] To date approximately 2 years of high vertical resolution longwave and shortwave radiative flux profiles

and corresponding heating rates consistent with CloudSat radar reflectivity observations have been processed and released to the general science community as CloudSat's level 2 fluxes and heating rates product. This paper serves to document the overall properties of the first year of this data through analysis of cloud impacts on TOA and surface radiative fluxes and atmospheric radiative heating. The first estimate of the annual mean Earth's radiation budget from CloudSat is generally consistent with those from other analyses and balances to within a 19 W m^{-2} surplus at the TOA. This is consistent with estimated measurement uncertainties in the products as well as the fact that CloudSat sampling does not extend poleward of 82° .

[37] A cursory analysis of cloud contributions to total atmospheric radiative heating suggest that cloud impacts on atmospheric heating are generally small on the global scale because of the competing effects of low cloud cooling that

dominates in polar regions and high cloud warming that pervades the tropics. On regional scales, however, cloud impacts can be much larger than the global mean and are often dominated by a particular type of clouds, simply defined here in terms of their CloudSat-defined tops. This suggests that small changes in the relative frequency of occurrence of these cloud types, such as those that may occur in a warmer climate, could exert a significant impact on regional energy balance.

[38] Independent uncertainty analyses using CERES and CALIPSO data suggest that SW fluxes are less certain than their LW counterparts and underscore the importance of accurately identifying low clouds that may be missed by CloudSat. Through the addition of MODIS-based cloud optical depth and effective radius information from CloudSat's soon to be released 2B-TAU product and additional cloud screening information provided by the combined radar-lidar cloud mask it is anticipated that these uncertainties will be significantly reduced in future versions of the algorithm. On the basis of comparisons with CERES TOA fluxes, however, it appears that the larger uncertainties characteristic of smaller time and space scales are, to large extent, random in nature and tend to average out considerably on the large spatial scales and annual time scales analyzed here. Thus despite the relatively short duration of the CloudSat mission to date, these early results demonstrate the potential for exploiting its vertically resolved radiative heating products to study cloud radiation feedbacks, assess the fidelity of longer-term observational data sets, and evaluate the representation of these processes in numerical models.

[39] **Acknowledgments.** This research was supported by NASA CloudSat Mission grant NAS5-99237 and NASA Energy and Water cycle Sponsored research (NEWS) grant NAG06GC46G. The authors thank the staff at the CloudSat Data Processing Center (DPC) and, in particular, Philip Partain for their assistance in implementing the FLXHR algorithm. All CloudSat data presented here were acquired through the DPC and can be accessed through their Web site <http://www.cloudsat.cira.colostate.edu>. The authors would also like to acknowledge Ed Eloranta and the University of Wisconsin Lidar Group (<http://lidar.ssec.wisc.edu/>) for graciously providing the AHSRL and MMCR data used in this study.

References

- Ba, M. B., R. Frouin, S. E. Nicholson, and G. Dedieu (2001a), Satellite-derived surface radiation budget over the African continent. Part I: Estimation of downward solar irradiance and albedo, *J. Clim.*, *14*, 45–58.
- Ba, M. B., S. E. Nicholson, and R. Frouin (2001b), Satellite-derived surface radiation budget over the African continent. Part II: Climatologies of the various components, *J. Clim.*, *14*, 60–76.
- Barkstrom, B. R. (1984), The Earth Radiation Budget Experiment (ERBE), *Bull. Am. Meteorol. Soc.*, *65*, 1170–1185.
- Bishop, J. K. B., W. B. Rossow, and G. Ellsworth (1997), Surface solar irradiance from the International Satellite Cloud Climatology Project 1983–1991, *J. Geophys. Res.*, *102*, 6883–6910.
- Breon, F.-M., R. Frouin, and C. Gautier (1994), Global shortwave energy budget at the Earth's surface from ERBE observations, *J. Clim.*, *7*, 309–324.
- Chen, T., W. B. Rossow, and Y. Zhang (2000), Radiative effects of cloud-type variations, *J. Clim.*, *13*, 264–285.
- Comstock, J. M., and K. Sassen (2001), Retrieval of cirrus cloud radiative and backscattering properties using combined lidar and infrared radiometer (LIRAD) measurements, *J. Atmos. Oceanic Technol.*, *18*, 1658–1673.
- Comstock, J. M., T. P. Ackerman, and G. G. Mace (2002), Ground-based lidar and radar remote sensing of tropical cirrus clouds at Nauru Island: Cloud statistics and radiative impacts, *J. Geophys. Res.*, *107*(D23), 4714, doi:10.1029/2002JD002203.
- Fu, Q., and K. N. Liou (1992), On the correlated k-distribution method for radiative transfer in nonhomogeneous atmospheres, *J. Atmos. Sci.*, *49*, 2139–2156.
- Gupta, S. K., W. F. Staylor, W. L. Darnell, A. C. Wilber, and N. A. Ritchey (1993), Seasonal variation of surface and atmospheric cloud radiative forcing over the globe derived from satellite data, *J. Geophys. Res.*, *98*, 20,761–20,778.
- Harries, J. E., et al. (2005), The Geostationary Earth Radiation Budget project, *Bull. Am. Meteorol. Soc.*, *86*, 949–960.
- Harrison, E. F., P. Minnis, B. R. Barkstrom, V. Ramanathan, R. D. Cess, and G. G. Gibson (1990), Seasonal variation of cloud radiative forcing derived from the Earth Radiation Budget Experiment, *Geophys. Res. Lett.*, *95*, 18,687–18,703.
- Hartmann, D. L. (1994), *Global Physical Climatology*, 411 pp., Academic, New York.
- Hartmann, D. L., and D. A. Short (1980), On the use of Earth radiation budget statistics for studies of clouds and climate, *J. Atmos. Sci.*, *37*, 1233–1250.
- Hartmann, D. L., M. Ockert-Bell, and M. L. Michelsen (1992), The effect of cloud type on Earth's energy balance: Global analysis, *J. Clim.*, *5*, 1281–1304.
- Hatzianastassiou, N., and I. Vardavas (2001), Shortwave radiation budget of the Southern Hemisphere using ISCCP C2 and NCEP-NCAR climatological data, *J. Clim.*, *14*, 4319–4329.
- Kandel, R., et al. (1998), The ScaRaB Earth radiation budget dataset, *Bull. Am. Meteorol. Soc.*, *79*, 765–783.
- Kiehl, J. T., and K. E. Trenberth (1997), Earth's annual global mean energy budget, *Bull. Am. Meteorol. Soc.*, *78*, 197–208.
- Lacis, A. A., and V. Oinas (1991), A description of the correlated-k distribution method for modeling nongray gaseous absorption, thermal emission, and multiple scattering in vertically inhomogeneous atmospheres, *J. Geophys. Res.*, *96*, 9027–9063.
- L'Ecuyer, T. S., and G. L. Stephens (2003), The tropical oceanic energy budget from the TRMM perspective. Part I: Algorithm and uncertainties, *J. Clim.*, *16*, 1967–1985.
- Lee, M.-I., I.-S. Kang, J.-K. Kim, and B. E. Mapes (2001), Influence of cloud-radiation interaction on simulating tropical intraseasonal oscillation with an atmospheric general circulation model, *J. Geophys. Res.*, *106*, 14,219–14,233.
- Li, Z., H. G. Leighton, K. Masuda, and T. Takashima (1993), Estimation of SW flux absorbed at the surface from TOA reflected flux, *J. Clim.*, *6*, 317–330.
- Liebmann, B., and D. L. Hartmann (1982), Interannual variations of outgoing IR associated with tropical circulation changes during 1974–1978, *J. Atmos. Sci.*, *39*, 1153–1162.
- Liou, K. N. (2002), *An Introduction to Atmospheric Radiation*, 2nd ed., 583 pp., Academic, New York.
- Lo, C., J. M. Comstock, and C. Flynn (2006), An atmospheric radiation measurements value-added product to retrieve optically thin cloud visible optical depths using micropulse lidar, *DOE/SC-ARM/TR-077*, U.S. Dep. of Energy, Washington, D. C.
- McFarlane, S. A., J. H. Mather, and T. P. Ackerman (2007), Analysis of tropical radiative heating profiles: A comparison of models and observations, *J. Geophys. Res.*, *112*, D14218, doi:10.1029/2006JD008290.
- Miles, N. L., J. Verlinde, and E. E. Clothiaux (2000), Cloud droplet size distributions in low-level stratiform clouds, *J. Atmos. Sci.*, *57*, 295–311.
- Miller, S. D., and G. L. Stephens (2001), CloudSat instrument requirements as determined from ECMWF forecasts of global cloudiness, *J. Geophys. Res.*, *106*, 17,713–17,733.
- Mitchell, D. L., A. Macke, and Y. Liu (1996), Modeling cirrus clouds. Part II: Treatment of radiative properties, *J. Atmos. Sci.*, *53*, 2967–2988.
- Moore, R. W., and T. H. Vonder Haar (2001), Interannual variability of cloud forcing and meridional energy transport for the Northern Hemisphere winter from 1984–1990, *J. Clim.*, *14*, 3643–3654.
- Ringer, M. A., and K. P. Shine (1997), Sensitivity of the Earth's radiation budget to interannual variations in cloud amount, *Clim. Dyn.*, *13*, 213–222.
- Ritter, B., and J.-F. Geleyn (1992), A comprehensive radiation scheme for numerical weather prediction models with potential applications in climate simulations, *Mon. Weather Rev.*, *120*, 303–324.
- Rossow, W. B., and A. A. Lacis (1990), Global, seasonal cloud variations from satellite radiance measurements. Part II: Cloud properties and radiative effects, *J. Clim.*, *3*, 1204–1253.
- Rossow, W. B., and Y.-C. Zhang (1995), Calculation of surface and top of the atmosphere radiative fluxes from physical quantities based on ISCCP data sets: 1. Validation and first results, *J. Geophys. Res.*, *100*, 1167–1197.
- Slingo, A., and J. M. Slingo (1988), The response of a general circulation model to cloud longwave radiative forcing. I: Introduction and Initial Experiments, *Q. J. R. Meteorol. Soc.*, *114*, 1027–1062.
- Slingo, J. M., and A. Slingo (1991), The response of a general circulation model to cloud longwave radiative forcing. II: Further studies, *Q. J. R. Meteorol. Soc.*, *117*, 333–364.

- Sohn, B.-J., and E. A. Smith (1992a), Global energy transports and the influence of clouds on transport requirements: A satellite analysis, *J. Clim.*, *5*, 717–734.
- Sohn, B.-J., and E. A. Smith (1992b), The modulation of the low-latitude radiation budget by cloud and surface forcing on interannual time scales, *J. Clim.*, *5*, 831–846.
- Sohn, B.-J., and E. A. Smith (1992c), The significance of cloud radiative forcing to the general circulation on climate time scales—A satellite interpretation, *J. Atmos. Sci.*, *49*, 845–860.
- Stackhouse, P. W., Jr., D. P. Kratz, G. R. McGarragh, S. K. Gupta, and E. B. Greer (2006), Fast longwave and shortwave flux (FLASHFlux) products from CERES and MODIS measurements, paper presented at 12th Conference on Atmospheric Radiation, Am. Meteorol. Soc., Madison, Wis. (Available at <http://ams.confex.com/ams/pdfpapers/113479.pdf>)
- Stephens, G. L., and T. J. Greenwald (1991a), The Earth's radiation budget and its relation to atmospheric hydrology. 1. Observations of the clear sky greenhouse effect, *J. Geophys. Res.*, *96*, 15,311–15,324.
- Stephens, G. L., and T. J. Greenwald (1991b), The Earth's radiation budget and its relation to atmospheric hydrology: 2. Observations of cloud effects, *J. Geophys. Res.*, *96*, 15,325–15,340.
- Stephens, G. L., P. W. Stackhouse Jr., and F. J. Flatau (1990), The relevance of the microphysical and radiative properties of cirrus clouds to climate and climate feedback, *J. Atmos. Sci.*, *47*, 1742–1753.
- Stephens, G. L., P. M. Gabriel, and P. T. Partain (2001), Parameterization of atmospheric radiative transfer. Part I: Validity of simple models, *J. Atmos. Sci.*, *48*, 3391–3409.
- Stephens, G. L., et al. (2002), The CloudSat mission and the A-Train: A new dimension of spacebased observations of clouds and precipitation, *Bull. Am. Meteorol. Soc.*, *83*, 1771–1790.
- Vonder Haar, T. H., and V. E. Suomi (1971), Measurements of the Earth's radiation budget from satellites during a five-year period. Part 1: Extended time and space means, *J. Atmos. Sci.*, *28*, 305–314.
- Weaver, C. P. (1999), Interactions among cyclone dynamics, vertical thermodynamic structure, and cloud radiative forcing in the North Atlantic summertime storm track, *J. Clim.*, *12*, 2625–2642.
- Wielicki, B. A., B. R. Barkstrom, E. F. Harrison, R. B. Lee III, G. L. Smith, and J. E. Cooper (1996), Clouds and the Earth's Radiant Energy System (CERES): An Earth Observing System experiment, *Bull. Am. Meteorol. Soc.*, *77*, 853–868.
- Wielicki, B. A., et al. (2001), Evidence for large decadal variability in the tropical mean radiative energy budget, *Science*, *295*, 841–844.
- Wu, D. L., J. H. Jiang, W. G. Read, R. T. Austin, C. P. Davis, A. Lambert, G. L. Stephens, D. G. Vane, and J. W. Waters (2008), Validation of the Aura MLS cloud ice water content measurements, *J. Geophys. Res.*, *113*, D15S10, doi:10.1029/2007JD008931.
- Zhang, Y.-C., W. B. Rossow, and A. A. Lacis (1995), Calculation of surface and top of the atmosphere radiative fluxes from physical quantities based on ISCCP data sets: 1. Method and sensitivity to input data uncertainties, *J. Geophys. Res.*, *100*, 1149–1165.

T. Haladay, T. S. L'Ecuyer, G. L. Stephens, and N. B. Wood, Department of Atmospheric Science, Colorado State University, Fort Collins, CO 80523, USA. (tristan@atmos.colostate.edu)

P. W. Stackhouse Jr., NASA Langley Research Center, Hampton, VA 23681, USA.